

Mesoporous Silica Nanoparticles for the Uptake of Toxic Antimony from Aqueous Matrices

Xiuzhen Yang, Bin Zhou, Changye Wang, Ronghao Tan, Shuangchan Cheng, Atif Saleem,* and Yuezhou Zhang*



Cite This: *ACS Omega* 2023, 8, 26916–26925

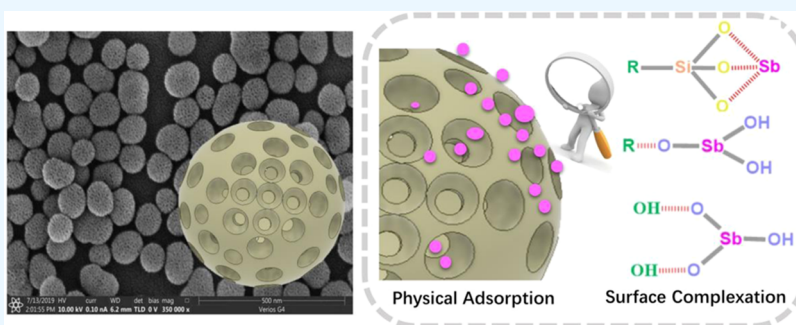


Read Online

ACCESS |

Metrics & More

Article Recommendations



ABSTRACT: Contamination of water sources by toxic antimony Sb(III) ions poses a threat to clean water supplies. In this regard, we have prepared a mesoporous silica nanoparticle (MSN)-derived adsorbent by reverse microemulsion polymerization, using cetyltrimethylammonium chloride (CTAC) and triethanolamine (TEA) as co-templates. The physical and chemical properties were characterized using advanced tools. The MSN exhibits a higher surface area of up to $713.72 \text{ m}^2 \cdot \text{g}^{-1}$, a pore volume of $1.02 \text{ cm}^3 \cdot \text{g}^{-1}$, and a well-ordered mesoporous nanostructure with an average pore size of 4.02 nm. The MSN has a high adsorption capacity for toxic Sb(III) of $27.96 \text{ mg} \cdot \text{g}^{-1}$ at pH 6.0 and 298 K. The adsorption data followed the Langmuir isotherm, while the kinetics of adsorption followed the pseudo-second-order model. Interestingly, the effect of coexisting iron showed a promoting effect on Sb(III) uptake, while the presence of manganese slightly inhibited the adsorption process. The recyclability of the MSN adsorbent was achieved using a 0.5 M HCl eluent and reused consecutively for three cycles with a more than 50% removal efficiency. Moreover, the characterization data and batch adsorption study indicated physical adsorption of Sb(III) by mesopores and chemical adsorption due to silicon hydroxyl groups.

1. INTRODUCTION

Water pollution poses a global threat to the biosphere and impacts the lives of millions of people worldwide. It is a leading global risk factor for illnesses, diseases, and fatalities while also diminishing the amount of safe drinking water accessible globally. Antimony Sb(III) is one of the toxic emerging pollutants of the 21st century.¹ It is a nonessential element of the human body, although it is widely used for a variety of industrial applications.² Anthropogenic activities such as ore mining and smelting lead to Sb(III) contamination in an aquatic environment. Sb(III) is well known for its toxicity and carcinogenic nature; therefore, it is listed as a priority contaminant by the Environmental Protection Agency of the United States (EPA US) and by the European Union (EU).³ Therefore, it is critical to develop more efficient and economical approaches for the removal of Sb(III) from contaminated water.

Currently, many technologies have been developed for Sb(III) removal from wastewater, such as coagulation⁴

bioremediation,⁵ membrane filtration,⁶ electrochemical deposition,⁷ and adsorption.⁸ Mostly, these approaches require high-end maintenance and energy; however, adsorption is most effective due to its low cost, simplicity, recyclability, and high efficiency.^{9–11} Many adsorbents have been developed so far for heavy metal ion adsorption from water, and these can be categorized as inorganic,^{1,12,13} organic,^{14–18} and biomass-derived.^{19–24} Activated carbon is a highly effective Sb(III) adsorbent due to its large surface area and porosity. However, it has been reported that the adsorption capacity of activated carbon decreases with increasing pH, which may limit its effectiveness in certain applications.²⁵ Iron oxide-based

Received: March 14, 2023

Accepted: June 30, 2023

Published: July 20, 2023



adsorbents, such as magnetite and hematite, have been found to be effective Sb(III) adsorbents due to their high adsorption capacity and stability in aqueous solutions. However, their efficiency may be impacted by the presence of competing ions, such as phosphate and sulfate, in water.²⁶ Recently, nanoscopic adsorbents have been paid increasing attention due to their unique physiochemical properties, particularly a high surface area and a mesoporous framework.^{13,27,28} Mesoporous silica nanoparticles (MSNs) are chemically inert, have a high surface area and abundant pores, and are decorated with functional groups.²⁹ However, their application as an adsorbent remains underdeveloped and needs further attention.³⁰ MSNs exhibit considerable potential as nanoadsorbents due to their unique combination of mesoporous and nanoscale materials. They possess a large specific surface area, adjustable pore size, easily modifiable surface functional groups, and a wide range of applications for effectively removing various heavy metal ions.^{31–33} Currently, several limitations regarding the facile synthesis of well-ordered MSNs and their efficient application for the removal of Sb(III) need to be addressed.³⁴

Herein, an MSN adsorbent was synthesized in a large quantity by reverse microemulsion polymerization using cetyltrimethylammonium chloride and triethanolamine as a co-template. The structure of MSNs was characterized by scanning electron microscopy (SEM), thermogravimetric analysis (TGA), X-ray diffraction (XRD), Brunauer–Emmett–Teller (BET), and Fourier transform infrared spectroscopy (FTIR). The adsorption performance of MSNs was investigated by adsorption kinetics, thermodynamics, effect of pH, and adsorbate dosage. Furthermore, the adsorption mechanism of Sb(III) on MSNs was analyzed and concluded. We envision that the study can provide a reference for well-ordered mesoporous nanoadsorbent synthesis and application for toxic Sb(III) uptake.

2. MATERIALS AND METHODS

2.1. Experimental Reagents. Sodium hydroxide (NaOH), hydrochloric acid (HCl), anhydrous ethanol (EtOH), dimethylformamide (DMF), manganese chloride tetrahydrate ($\text{MnCl}_2 \cdot 4\text{H}_2\text{O}$), anhydrous calcium chloride (CaCl_2), sodium chloride (NaCl), tetraethyl orthosilicate (TEOS), cyclohexane, cetyltrimethylammonium chloride (CTAC), triethanolamine (TEA), ammonium nitrate (NH_4NO_3), and antimony potassium tartrate ($\text{C}_8\text{H}_8\text{K}_2\text{O}_{12}\text{Sb}$) are all analytical reagent and used without further treatment.

2.2. Preparation of Materials. MSNs were prepared according to a previous method³⁵ with few modifications. Dendritic MSNs were prepared via a one-pot biphasic stratification approach by continuous growth using cationic surfactant CTAC as a template, TEOS as a silica source, TEA as a catalyst, and an organic solvent such as cyclohexane as an emulsion agent. At first, 24 mL of (25 wt %) CTAC solution and 0.18 g of TEA were added to 36 mL of water and stirred gently at 60 °C for 1 h in a 100 mL round-bottom flask. Afterward, 16 mL of TEOS and 20 mL of cyclohexane were carefully added into the (CTAC–TEA) aqueous solution, and the mixture was kept at 60 °C in an oil bath under magnetic stirring. The reaction was then kept at a constant temperature with continuous stirring for 12 h to obtain the final products. After removing the upper oil phase, the lower layer was separated.

The products were collected by centrifugation and washed several times with ethanol to remove the residual reactants.

Then, the template was extracted with 0.6 wt % ammonium nitrate (NH_4NO_3) in EtOH at 60.0 °C for 6 h. The resulting product was a white powder, which was stored in a dry place.

2.3. Characterization. The surface functional binding sites were studied by Fourier transform infrared (FTIR) spectroscopy to further characterize the sample using a Thermo Nicolet 360 instrument in Nicolet. The powder X-ray diffraction (XRD) patterns were recorded on a Bruker D4 X-ray diffractometer in Germany using Ni-filtered Cu KR radiation (40 kV, 40 mA). X-ray photoelectron spectroscopy (XPS) spectra were obtained at room temperature using a JPS-9010TR (JEOL) instrument with a Mg $K\alpha$ X-ray source. The sample was compressed into films with KBr under reduced pressure before XPS analysis. The organic polymer contents were determined by thermogravimetric analysis (TGA, NETZSCHSTA 409 TG-DTA, Germany). A Micromeritics Tristar 3000 analyzer was used to measure nitrogen adsorption–desorption isotherms at 77 K. Prior to the measurements, the samples underwent degassing in vacuum at 180 °C for 10 h. Specific surface areas were calculated using the Brunauer–Emmett–Teller (BET) method within a relative pressure range of 0.005–0.25. Pore volumes and pore size distributions were determined from the adsorption branches of isotherms using the Barrett–Joyner–Halenda (BJH) model. Total pore volumes (V_i) were estimated from the amount adsorbed at a relative pressure P/P_0 of 0.995. A flame atomic spectrometer (Perkin Elmer Analyst 400) was used to analyze the Sb(III) concentration.

2.4. Adsorption Experiment. In this experiment, $\text{C}_8\text{H}_8\text{K}_2\text{O}_{12}\text{Sb}$ was used as the source of Sb(III). The quantitative chemicals were weighed and dissolved in a beaker (HCl-assisted dissolution) and then transferred to a 1000 mL volumetric flask. A 1000 $\text{mg}\cdot\text{L}^{-1}$ stock was prepared. In order to study the adsorption performance of MSNs for Sb(III) in water, the relationship among time, pH, the initial concentration of the solution, and adsorption capacity was investigated (all experimental data were measured by standing the solution for 30 min, filtering by a 0.4 μm filter head, and then measuring by an atomic flame spectrometer).

2.4.1. Adsorption Kinetics. The dosage of MSNs was 130 mg, the initial concentration and volume of Sb(III) solution were 10 $\text{mg}\cdot\text{L}^{-1}$ and 100 mL, respectively, the pH was adjusted to 6.0, the temperature and speed of the constant temperature oscillation box were set at 298 K and 150 rad/min, respectively, and 10 mL of Sb(III) solution was sampled every specific time.

2.4.2. Adsorption Thermodynamics. The dosage of MSNs was 130 mg, the volume of Sb(III) solution was 100 mL, the pH was adjusted to 6.0, the rotational speed was set to 150 $\text{rad}\cdot\text{min}^{-1}$, the reaction temperatures were set to 298, 308, and 318 K, the initial concentrations were 10, 20, 50, 100, 150, and 200 $\text{mg}\cdot\text{L}^{-1}$, and the reaction contact time was 480 min.

2.4.3. pH Effect. For the experiment, the dosage of MSNs used was 130 mg and the volume of Sb(III) solution was 100 mL. The pH value was adjusted to 1.5, 3.0, 4.5, 6.0, 7.5, 9.0, and 10.5. The water bath constant temperature oscillation box maintained a temperature of 298 K and a rotation speed of 150 rpm. The reaction contact time was 480 min.

2.4.4. Effect of Coexisting Ions. To investigate the impact of coexisting ions, 130 mg of MSNs were used, and the initial volume of Sb(III) solution was 100 mL with a concentration of 10 $\text{mg}\cdot\text{L}^{-1}$. The initial concentrations of Fe^{3+} and Mn^{2+} ions were 0.1, 1.0, and 5.0 $\text{mg}\cdot\text{L}^{-1}$, with a pH value of 6.0. The

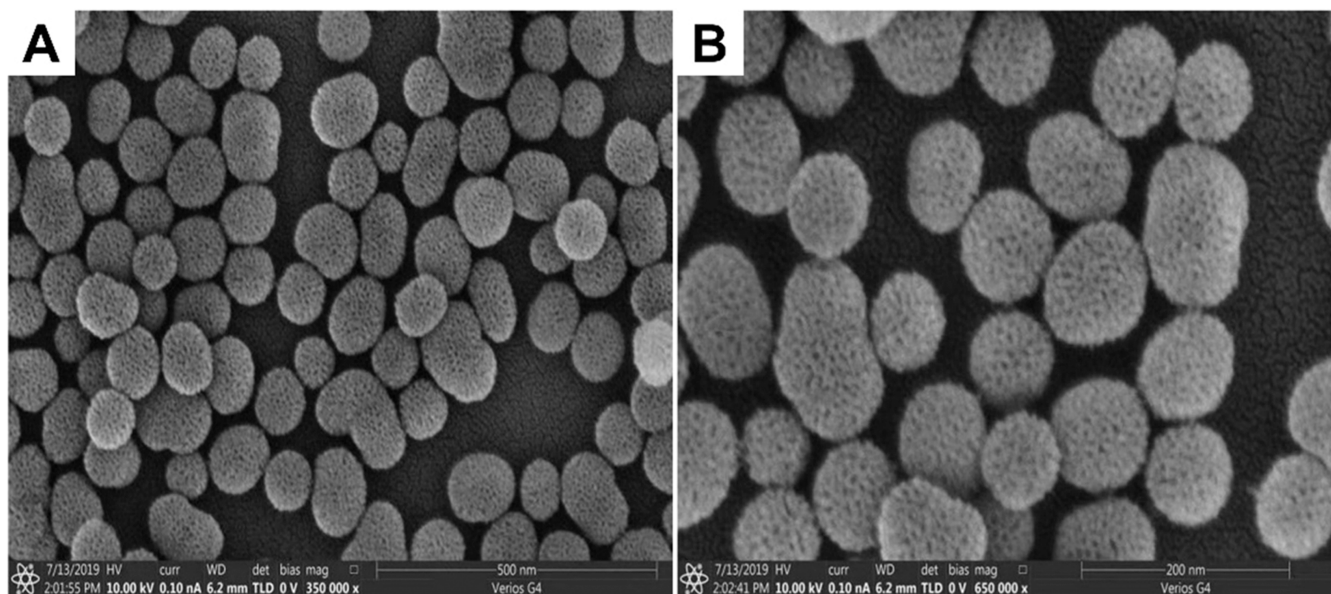


Figure 1. (A) Scanning electron microscopy (SEM) images of MSN at lower magnification and (B) SEM image at higher magnification.

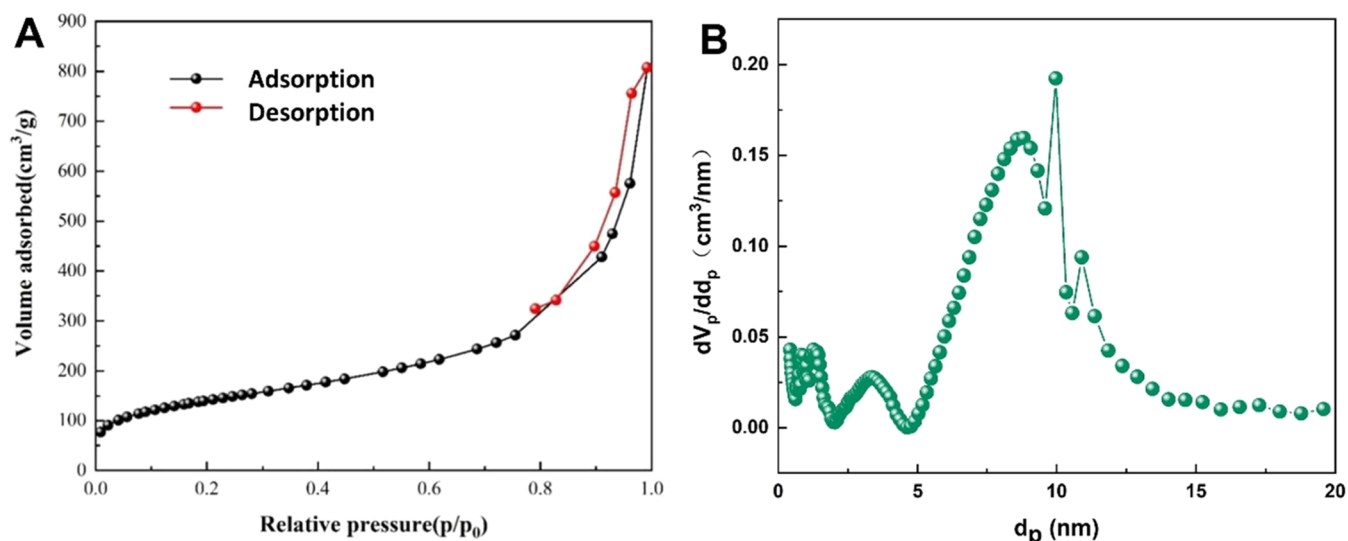


Figure 2. (A) Nitrogen adsorption–desorption isotherms and (B) pore size distribution.

water bath constant temperature oscillation box maintained a temperature of 298 K and a rotation speed of 150 rpm. The adsorption contact time was 480 min.

2.4.5. Regeneration Experiment. 130 mg of adsorbed heavy metal ions were dried at 50 °C and then added to 100 mL of a 0.5 M hydrochloric acid desorption solution. Under the conditions of 298 K and 300 rpm, the material was shaken at a constant temperature for 24 h. After repeated ultrasonic cleaning with pure water, the material was centrifuged and dried under vacuum. The regeneration of mesoporous silica nanoparticles was studied.

3. RESULTS AND DISCUSSION

3.1. Characterization of MSNs. Figure 1A illustrates the structural characteristics and morphology of the MSN adsorbent. The particles exhibit nearly uniform gradient morphology and possess rough surfaces with a shape resembling that of a strawberry. Notably, the MSNs display a highly organized mesoporous structure. Upon closer examina-

tion at higher magnification (as depicted in Figure 1B), it can be observed that the large pores resembling a cage are situated in the central core, while smaller channels arranged in a honeycomb pattern are distributed radially throughout the outer shell.

Nitrogen adsorption and desorption analysis of MSN showed typical type-IV peaks with a unique capillary condensation step at relatively high pressures of $0.8 < P/P_0 < 1.0$ (Figure 2A). The data showed obvious hysteresis loops, which confirms that MSNs have a mesoporous framework.³⁶ At low pressure of near 0, nitrogen adsorption also occurs, implying the presence of micropores. The adsorption capacity of nitrogen in the first half slowly increases with the increase of P/P_0 . In the low-pressure region, the nitrogen adsorption capacity of MSNs is linearly improved and nitrogen molecules are adsorbed on the inner surface of the mesopores as a single layer. MSNs have a rapid increase process when the relative pressure is $0.6 < P/P_0 < 0.8$ because the capillary pores condense the nitrogen molecules to fill the mesopores. When

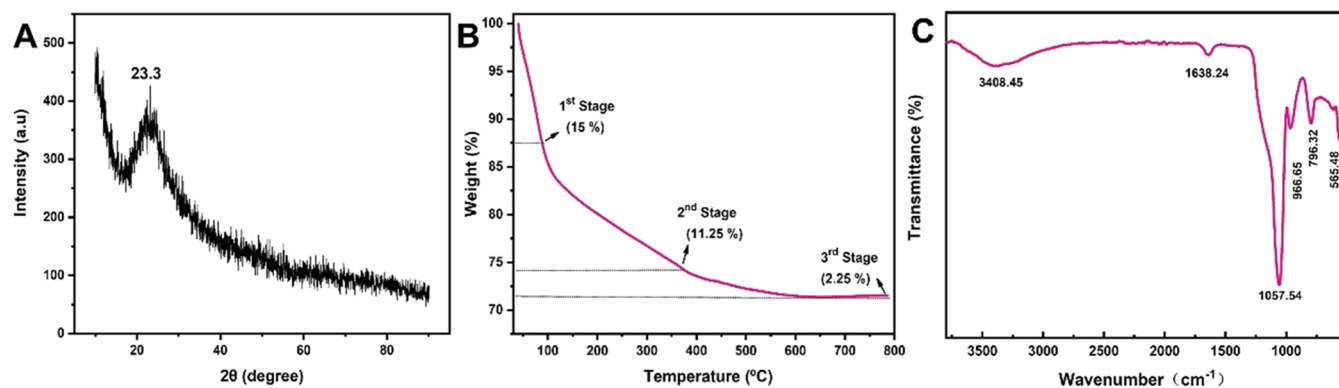


Figure 3. (A) X-ray diffraction analysis of MSN, (B) thermogravimetric analysis of MSN, and (C) Fourier transform infrared spectrum of MSN.

P/P_0 is higher than 0.8, a clear hysteresis loop appears. At this stage, the nitrogen molecules are mainly adsorbed on the outer surface of the mesoporous material in a monolayer. The specific surface area and total pore volume are calculated to be $713.72 \text{ m}^2\cdot\text{g}^{-1}$ and $1.02 \text{ cm}^3\cdot\text{g}^{-1}$, respectively. The pore size distribution was calculated by the Barrett–Joyner–Halenda (BJH) approach (Figure 2B). The average pore size determined by the BJH method was 4.02 nm, which confirms the mesoporous nature of MSN.

The crystalline phase composition of MSN was investigated by X-ray diffraction (XRD) analysis and the results can be seen in Figure 3A. The diffraction pattern shows typical characteristic peaks of MSNs near 23.3, indicating the amorphous nature of the MSNs, which is consistent with the literature.³⁷ Thermogravimetric analysis (TGA) was determined to evaluate the decomposition rate and phase transition of MSN, and the results are shown in Figure 3B. The weight loss occurred in three stages: (i) physical desorption, (ii) inner surface weight loss, and (iii) hydroxyl group desorption stage. In the first stage, 15% weight loss occurred within 100 °C, which was due to the loss of large quantities of physically adsorbed water. As the temperature increased to 390 °C, a further 11.3% weight loss was observed in the second stage, which was due to the inner surface shrinkage and desorption of silicon hydroxyl functional moieties. Furthermore, as the temperature increased from 390 to 625 °C, a weightlessness of 2.25% was observed, which could be due to the desorption of hydroxyl groups and polymerization of silanol functional sites. After 625 °C, MSNs no longer desorbed water or organic matter, and the residual pure silicon oxide exhibited good thermal stability.

Fourier transform infrared spectroscopy (FTIR) was used to determine the chemical state of functional groups present on the MSN surface. As can be seen in Figure 3C, there is no C–H adsorption peak around $2800\text{--}3000 \text{ cm}^{-1}$, which interpret as the complete removal of the template during a successful MSN synthesis process. The IR spectra of MSNs show characteristic peaks at 3408 and 1638 cm^{-1} , which are individually assigned to the stretching and bending vibrations of –OH and H–OH groups, respectively.³⁸ The peaks appearing at 1058 and 967 cm^{-1} represent the stretching vibrations of Si–O–Si and Si–OH, respectively. In addition, the peaks at 796 and 565 cm^{-1} are attributed to the bending vibrations of Si–O–Si and Si–OH, respectively.^{39–43}

3.2. Batch Adsorption Study. 3.2.1. Effect of Solution pH. Solution pH is a very critical parameter of the adsorption process, since it controls the metal speciation and surface

charge of the adsorbent. Sb(III) has an identical s^2p^3 outer orbital electron configuration; therefore, it exists in different oxidation states (–III, 0, +III, and +V) under a wide range of pH. Figure 4 represents Sb(III) removal by MSNs in the pH

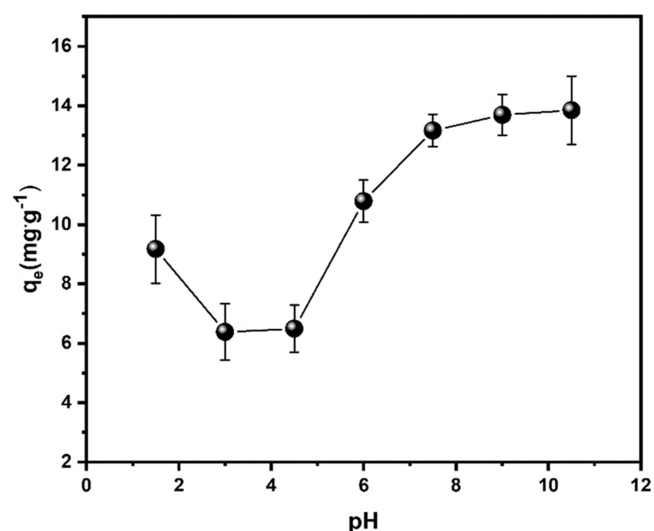


Figure 4. Effect of pH on adsorption performance (MSNs, 130 mg; Sb(III) concentration, $10 \text{ mg}\cdot\text{L}^{-1}$; contact time, 8 h; stirring speed, 150 rpm).

range of 1.5–10.5. At acidic conditions ($\text{pH} = 1.5$), mainly cationic forms (SbO^+ and $\text{Sb}(\text{OH})^{2+}$) of Sb(III) exist, and the adsorption capacity by MSNs is $9.17 \text{ mg}\cdot\text{g}^{-1}$. The low adsorption performance at acidic pH is due to the competition between H^+ and cationic forms of Sb(III) for adsorption sites. The adsorption capacity increases slightly with an increase in pH from 2.0 to 10.4, while a maximum adsorption of $13.85 \text{ mg}\cdot\text{g}^{-1}$ took place at $\text{pH} = 10.5$. The increase in the adsorption performance of MSNs was mainly due to electrostatic interaction among the changing oxidation states of Sb(III) from an acidic to a basic environment (H_2SbO_3^- , $\text{Sb}(\text{OH})_3$, $\text{Sb}(\text{OH})_4^-$, and H_2SbO_4^-). At $\text{pH} 2\text{--}10.4$, Sb(III) ions in water mainly exist in the form H_2SbO_3^- and $\text{Sb}(\text{OH})_3$ molecular states. The adsorption capacity of MSNs for Sb(III) removal increases with the increase of pH due to deprotonation of adsorbent sites and changing oxidation states of antimony. When the pH value of water is 10.5, Sb(III) ions in the water mainly exist in the form of $\text{Sb}(\text{OH})_4^-$ and H_2SbO_4^- , and the adsorption capacity reaches up to $13.85 \text{ mg}\cdot\text{g}^{-1}$.

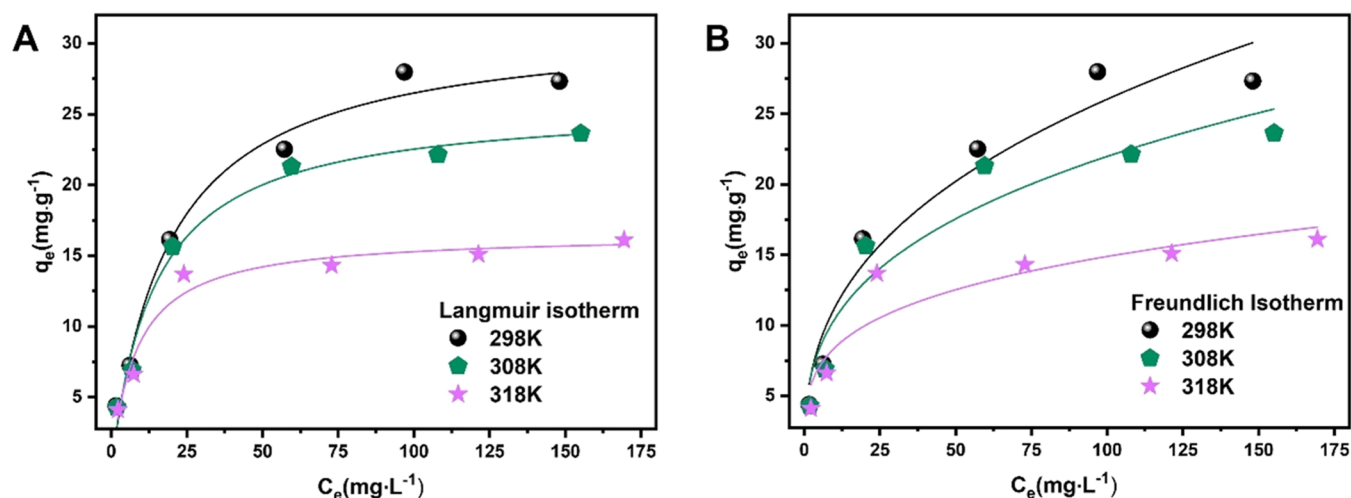


Figure 5. (A) Langmuir adsorption isotherm fitting. (B) Freundlich adsorption isotherm fitting (initial Sb(III) concentration: 10–200 mg·L⁻¹; adsorbent concentration: 130 mg; equilibrium time: 480 min; temperature: 298–318 K, agitation speed: 150 rpm, and pH: 6.0 ± 0.1).

3.2.2. Adsorption Isotherm Study. Figure 5 represents the MSN adsorption performance for toxic Sb(III) ions. The adsorption capacity of Sb(III) gradually increased as the equilibrium concentration increased, eventually tending to be saturated due to the mass transfer of Sb(III) ions from the aqueous phase to adsorbent active sites. The maximum equilibrium adsorption capacities of Sb(III) at 298, 308, and 318 K were 27.96, 22.13, and 15.09 mg·g⁻¹, respectively, at pH 6.0. The increase of temperature is not favorable to the adsorption reaction, causing a decrease in the adsorption performance of MSNs. Table 2 represents the comparative analysis of the adsorption performance and surface morphology of MSNs with a silica-derived adsorbent from the previously reported literature. As can be seen, the overall MSN adsorption performance and surface morphological characteristics were superior to those of reported adsorbents.

Langmuir and Freundlich isotherm models were used to simulate the adsorption behavior of MSNs for Sb(III) ions. The adsorption data were simulated by isotherm models to explain the mechanism of adsorption. The Freundlich isotherm is represented in eq 1

$$q_e = k_F \cdot C_e^{1/n} \quad (1)$$

The Langmuir isotherm is expressed in eq 2.

$$q_e = \frac{q_m k_L C_e}{1 + k_L C_e} \quad (2)$$

where C_e (mg·L⁻¹) and q_e (mg·g⁻¹) are the equilibrium concentration and adsorption capacity, q_m (mg·g⁻¹) is the calculated maximum adsorption capacity, while b (L·mg⁻¹) is the affinity constant, k_f (L·mg⁻¹) is the Freundlich isotherm constant, and $1/n$ represents the heterogeneous surface.

The parameters of the simulation curve are shown in Table 1. The R^2 values of the Langmuir isotherm model at 298, 308, and 318 K were 0.9801, 0.9825, and 0.9569, respectively, which are higher than Freundlich isotherm R^2 values of 0.9402, 0.9080, and 0.8395, respectively. The fitting degree of Langmuir's nonlinear regression is higher, which indicates monolayer adsorption. The MSN exhibited superior surface properties and heavy metal adsorption compared to the other silica-derived adsorbents listed in Table 2.

Table 1. Simulated Parameters of Langmuir and Freundlich Isotherms for Sb(III) Adsorption on MSNs at pH 6.0 ± 0.1

| T (K) | Langmuir isotherm | | | Freundlich isotherm | | |
|-------|-------------------|--------|--------|---------------------|--------|--------|
| | Q_0 (mg/g) | K_L | R^2 | K_F | $1/n$ | R^2 |
| 298 | 31.4548 | 0.0534 | 0.9801 | 4.8425 | 0.3652 | 0.9402 |
| 308 | 25.7705 | 0.0695 | 0.9825 | 4.9442 | 0.3240 | 0.9080 |
| 318 | 16.5498 | 0.1212 | 0.9569 | 4.7332 | 0.2488 | 0.8395 |

3.2.3. Adsorption Kinetics. The adsorption kinetic parameters are very important to determine the rate-limiting steps, adsorption mechanism, and mass transfer. Figure 6 shows the adsorption kinetics of Sb(III) ions from an aquatic environment at 298 K. It can be observed that the adsorption rate increases rapidly in the first 120 min; as the adsorption time interval continues to extend, the adsorption rate gradually slows down, and finally the equilibrium point is attained in both states. After 400–600 min, the adsorption process has basically been balanced, attaining the maximum equilibrium adsorption capacity. This could be due to the availability of a large number of adsorption sites and an ordered mesoporous structure.

In order to deeply explore the kinetic adsorption process, the pseudo-first-order kinetic and pseudo-second-order kinetic equations were used to analyze the adsorption dynamics data. The pseudo-first-order kinetic and pseudo-second-order kinetic models are shown in eqs 3 and 4, respectively.

$$q_t = q_e (1 - e^{-k_1 t}) \quad (3)$$

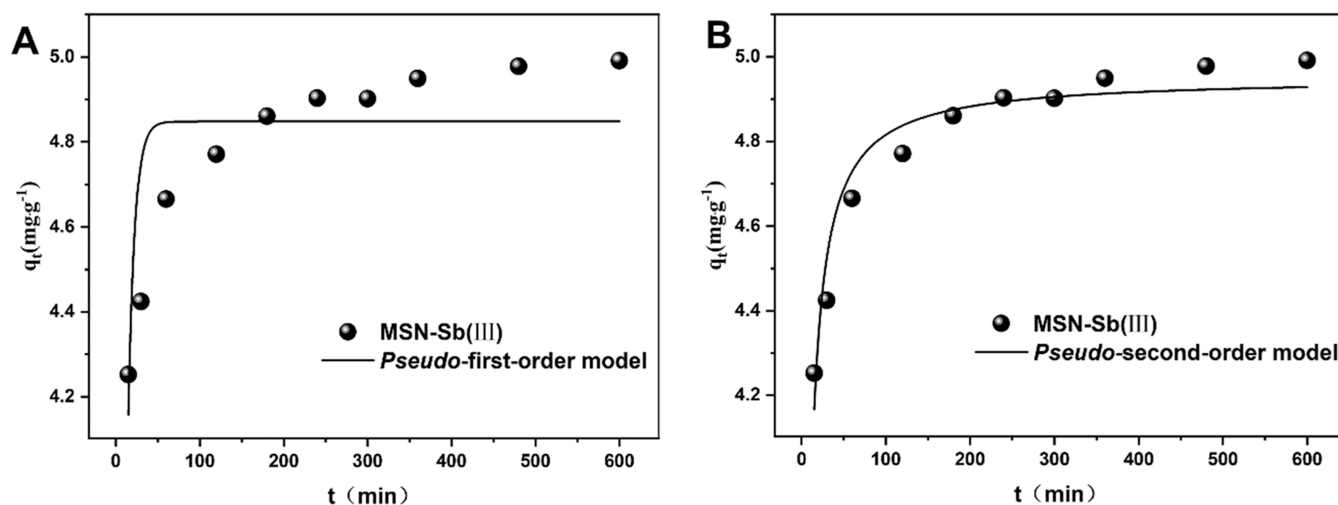
$$\frac{t}{q_t} = \frac{1}{k_2 q_e^2} + \frac{t}{q_e} \quad (4)$$

where q_t represents the adsorption amount at time t , q_e (mg·g⁻¹) is the adsorption amount at the equilibrium state (mg·g⁻¹), k_1 (min⁻¹) is a constant related to the pseudo-first-order model, and k_2 (g·mmol⁻¹ min⁻¹) is the second-order constant.

The fitting parameters are illustrated in Table 3, indicating that the R^2 of the pseudo-second-order kinetic model is 0.93, which is much higher than that of the pseudo-first-order kinetic model (0.59). Therefore, pseudo-second-order kinetics is more suitable to describe the adsorption of Sb(III) by MSNs, which indicates the chemical nature of the adsorption

Table 2. Comparison of the Effect of the Same Type of Mesoporous Silica Adsorbent in Removing Different Heavy Metal Ions

| adsorbents | removal ions | absorption capacity $\text{mg}\cdot\text{g}^{-1}$ | specific area $\text{m}^2\cdot\text{g}^{-1}$ | pore size nm | references |
|---|------------------|---|--|--------------|------------|
| TMMS | Cd^{2+} | 33.33 | 405.67 | 4.86 | 44 |
| mesoporous silica-cross-linked chitosan composite | Pb^{2+} | 97.8 | 302.49 | 2–3 | 45 |
| MSM | Pb^{2+} | 38.91 | 711.95 | 3.27 | 46 |
| sSiO ₂ @V-SiO ₂ | Cd^{2+} | 25.00 | 29.00 | | 47 |
| MMS | Sb^{3+} | 17.86 | 581.77 | 4.58 | 48 |
| MSNs | Sb^{3+} | 31.45 | 713.72 | 4.02 | this study |

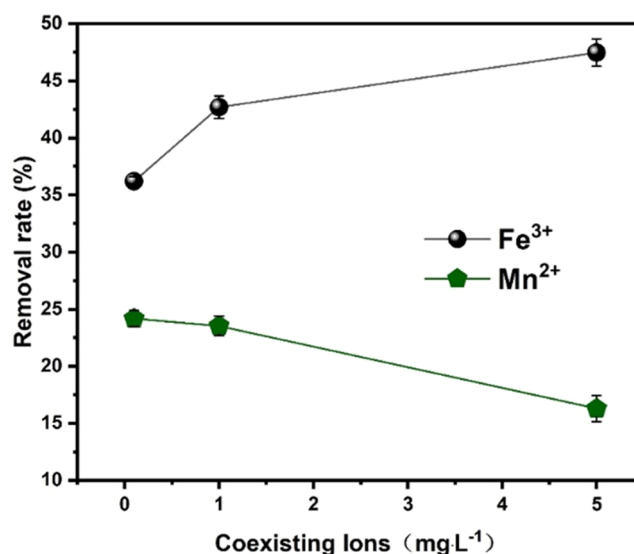
Figure 6. (A) Pseudo-first-order kinetic model fitting; (B) pseudo-second-order kinetic model fitting (initial Sb(III) concentration: $10 \text{ mg}\cdot\text{L}^{-1}$; adsorbent concentration: 130 mg ; equilibrium time: $0\text{--}600 \text{ min}$; temperature: 298 K ; agitation speed: 150 rpm , and $\text{pH}: 6.0 \pm 0.1$).Table 3. Simulated Kinetic Parameters of Sb(III) Ion Adsorption on MSNs Fitted by Pseudo-First-Order and Pseudo-Second-Order Models at $\text{pH} 6.0 \pm 0.1$ and 298 K

| pseudo-first-order model | | | pseudo-second-order model | | |
|------------------------------|-----------------------------|-------|------------------------------|---|-------|
| Q_e (mg g^{-1}) | k_1 (min^{-1}) | R^2 | Q_e (mg g^{-1}) | K_2 ($\text{g mg}^{-1}\text{min}^{-1}$) | R^2 |
| 4.848 | 0.129 | 0.59 | 4.951 | 0.071 | 0.938 |

process. Furthermore, the structural properties of MSNs play a significant role in determining the adsorption kinetics. The high surface area, pore volume, and mesoporous framework with an abundance of hydroxyl binding sites provided an ideal platform for the adsorption of Sb(III) ions, and the chemical nature of the adsorption process can be attributed to the formation of chemical bonds among Sb(III) and functional groups of MSNs.

3.2.4. Effects of Coexisting Ions. The effect of coexisting ions on the removal of Sb(III) by MSNs was systematically investigated to evaluate the adsorption performance of the adsorbent from a complex wastewater environment. As shown in Figure 7, when iron and Sb(III) ions coexist, iron ions have a synergistic effect on the removal of Sb(III). However, the mixed solution of Mn and Fe inhibits the removal rate of Sb(III) ions, and the maximum uptake can reach only up to $0.61 \text{ mg}\cdot\text{g}^{-1}$. This could be due to the competition among Sb(III) ions and Mn(II) for adsorption sites, specific ionic potential, and smaller hydrated ionic radius.¹³ Therefore, the manganese ion is the competitive ion for MSNs to remove Sb(III) from aqueous matrices.

3.2.5. Regeneration Experiment. For the long-term efficient application of the MSN adsorbent, the regeneration study of Sb(III)-adsorbed MSNs was conducted in a $0.5 \text{ M}\cdot\text{L}^{-1}$ HCl solution, and the results are illustrated in Figure 8. It can be

Figure 7. Effect of coexisting cations (Fe^{3+} and Mn^{2+}) on the removal of Sb(III) by MSNs (initial Sb(III) concentration: $10 \text{ mg}\cdot\text{L}^{-1}$; adsorbent concentration: 130 mg ; temperature: 298 K ; equilibrium time: 480 min ; coexisting ion concentrations: $0.1\text{--}5.0 \text{ mg}\cdot\text{L}^{-1}$).

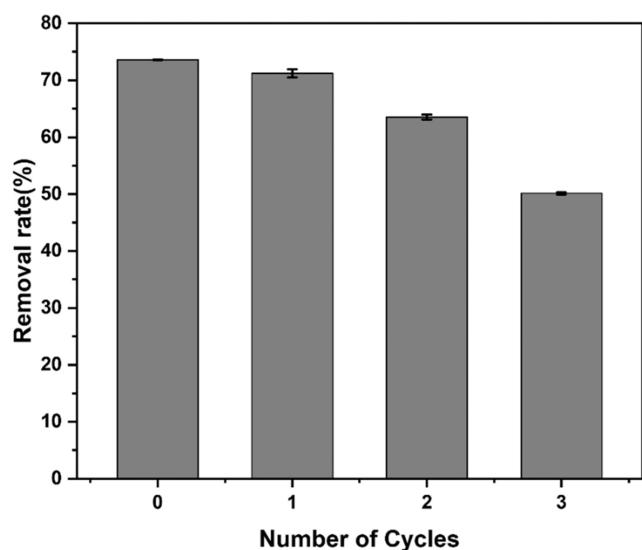


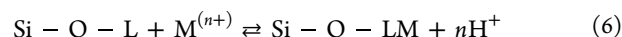
Figure 8. Effects of regeneration times on adsorbent regeneration.

observed that the removal rate reduced to 71.21% after the first cycle of regeneration, while the removal rate reduced to 50.14% after the third adsorption regeneration cycle. This could be because part of Sb(III) originally adsorbed on the active sites has not been completely desorbed, resulting in a relative decrease in the number of binding sites on the surface of the adsorbent. In addition, the desorbing acid could destroy the mesoporous structure of MSNs, which results in the decrease of the physical adsorption of Sb(III). The regeneration process of the adsorbent has a great influence on the pore and specific surface area of MSNs and also on the chemical structure of the adsorbent. Therefore, the adsorption effect of regenerated MSNs is reduced.

3.3. Adsorption Mechanism. The investigation of the adsorption mechanism of Sb(III) ions is one of the fundamental processes to elucidate the knowledge gap between the design and synthesis of the adsorbent for targeted removal application. FTIR and XPS analyses were conducted to confirm the adsorption of Sb(III) onto MSN. Prior to freeze

drying, the solid samples containing the adsorbed Sb(III) were washed with Milli-Q water to remove physically and loosely bound Sb(III) from the adsorbent surface. The FTIR analysis was utilized to detect changes in functional groups before and after Sb(III) adsorption. Three primary differences were observed in the spectrum pattern of MSN, as presented in Figure 9A. Notably, the peak at 3408 cm^{-1} , attributed to the stretching vibration of -OH , shifted to 3376 cm^{-1} , indicating that surface complexation between Sb(III) and OH^- functional groups was responsible for the adsorption of Sb(III) onto the MSN surface. Moreover, the peak at 1638 cm^{-1} , assigned to the stretching vibrations of silicon hydroxyl groups, shifted to 1637 cm^{-1} , demonstrating that oxygen-containing silicon hydroxyl functional groups contributed to Sb(III) adsorption. XPS analysis was employed to study the adsorption mechanism, as shown in Figure 9B. The obtained survey scan of MSNs after Sb(III) adsorption revealed the presence of Sb 3d species, which is in accordance with previously reported studies.

As shown in Figure 10, the removal of Sb(III) ions took place due to inner sphere exchange and coordination complex formation due to the presence of silicon hydroxyl groups on the surface of the adsorbent. The chemical reaction that took place was further illustrated in eqs 5 and 6. According to characterization analysis, the MSN surface had plenty of Lewis bases, which chelated with Sb(III) ions by sharing electron pairs and formed a coordination complex.



According to the kinetics, thermodynamics studies, SEM, FTIR, and other characterization, it can be seen that the adsorption of Sb(III) by MSN is mainly due to chemisorption. The nitrogen adsorption/desorption analysis indicated the presence of few micropores on the surface of the adsorbent, which can improve the removal of Sb(III). At different pH conditions, the products are different, including $(\text{R-O})_3\text{-Sb}$, R-O-Sb-(OH)_2 , and R-O-Sb=O . Under acidic conditions, the existence of a large number of hydrogen ions in the solution is not conducive to ion adsorption, whereas under

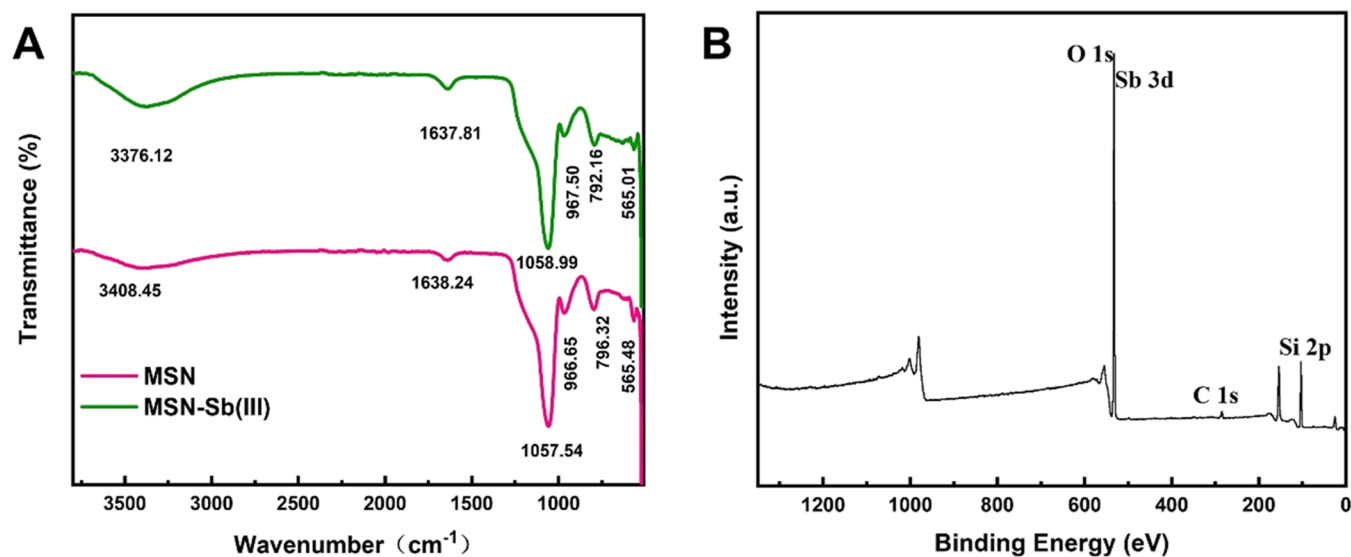


Figure 9. (A) FTIR spectrum of MSNs before and after Sb(III) adsorption. (B) XPS wide survey spectrum of MSNs after Sb(III) adsorption.

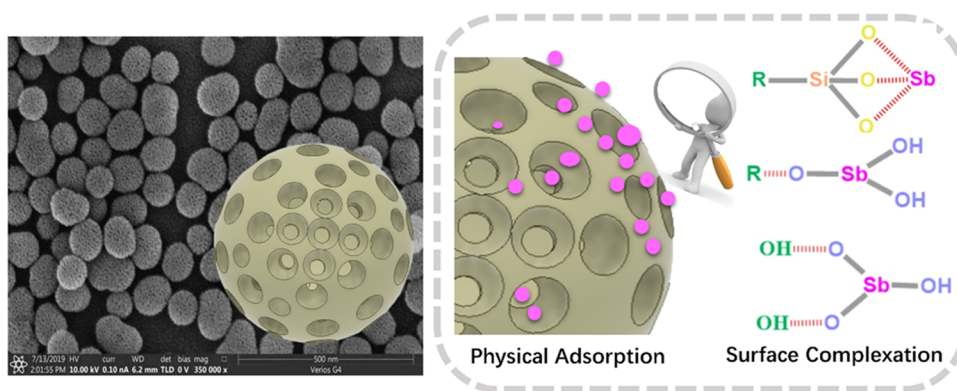
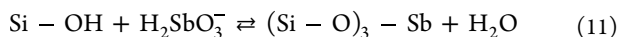
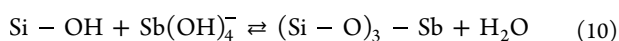
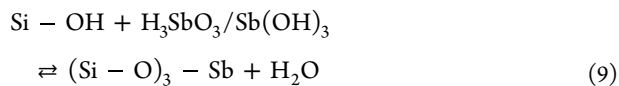
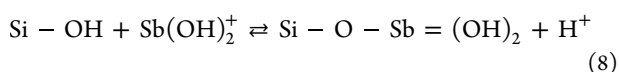
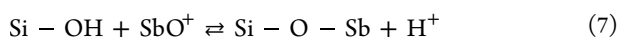


Figure 10. Removal mechanism of Sb(III) by MSNs.

alkaline conditions, the silicon hydroxyls are deprotonated, which favors the Sb(III) ions' adsorption.



As shown in Figure 10, the adsorption reactions of Sb(III) ions on the inner surface of MSNs at different pH values are varied. It can be seen from Figure 9 that with the change in pH, the adsorption effect of MSNs is concave, which is mainly caused by the existing form of Sb(III) ions and the effect of hydrogen ions in the solution. When $\text{pH} < 2$, the silicon hydroxyl group on the inner surface of the adsorbent reacts with SbO^+ to form R-O-Sb=O , and the silicon hydroxyl group reacts with Sb(OH)_2^+ to form R-O-Sb(OH)_2 . Under strong acidic conditions, the covalent bond of Sb(OH) breaks to form $(\text{R-O})_3-\text{Sb}$, leading to the adsorption move rightward.

4. CONCLUSIONS

In summary, mesoporous silica nanoparticles (MSNs) exhibiting well-ordered morphology were prepared by a reverse microemulsion polymerization approach using cetyltrimethylammonium chloride (CTAC) and triethanolamine (TEA) as co-templates. The as-prepared MSNs were characterized and successfully used as an adsorbent for the removal of toxic Sb(III) ions from water matrices. The systematic adsorption experiment data followed the Langmuir isotherm, with a maximum adsorption capacity of $31.45 \text{ mg}\cdot\text{g}^{-1}$ at 298 K, while the kinetics of adsorption was well defined by the pseudo-second-order model. The study also shows that the pH of the solution affects the adsorption of Sb(III) by MSNs, with strong alkaline conditions being the most effective. Furthermore, it is observed that the adsorption and removal of heavy metal ions by MSNs is achieved mainly through ion exchange with hydroxyl groups on the inner surface. Overall, these findings suggest that MSNs have potential as an effective adsorbent material for heavy metal ions in water treatment applications and can be produced at a larger scale.

AUTHOR INFORMATION

Corresponding Authors

Atif Saleem – Frontiers Science Center for Flexible Electronics and MIIT Key Laboratory of Flexible Electronics (KLoFE), Institute of Flexible Electronics Northwestern Polytechnical University, Xi'an 710072, China; orcid.org/0000-0002-2240-3252; Email: Atif@nwpu.edu.cn

Yuezhou Zhang – Frontiers Science Center for Flexible Electronics and MIIT Key Laboratory of Flexible Electronics (KLoFE), Institute of Flexible Electronics Northwestern Polytechnical University, Xi'an 710072, China; orcid.org/0009-0000-7497-1916; Email: zyezhou@126.com

Authors

Xiuzhen Yang – College of Civil Engineering, Hunan University of Science and Technology, Xiangtan 411201, China

Bin Zhou – College of Civil Engineering, Hunan University of Science and Technology, Xiangtan 411201, China

Changye Wang – College of Civil Engineering, Hunan University of Science and Technology, Xiangtan 411201, China

Ronghao Tan – 3RD Construction CO. LTD of China Construction 5th Engineering Bureau Changsha, Changsha 410004, China

Shuangchan Cheng – College of Civil Engineering, Hunan University of Science and Technology, Xiangtan 411201, China

Complete contact information is available at: <https://pubs.acs.org/10.1021/acsomega.3c01735>

Author Contributions

R.T. and B.Z. performed the experiments. S.C. and C.W. analyzed data. X.Y. and Y.Z. conceptualized the project and prepared the manuscript.

Notes

The authors declare no competing financial interest.

ACKNOWLEDGMENTS

This study was funded by the National Natural Science Foundation of China (grant number 51604113), the Natural Science Foundation of Hunan Province (grant number 2019JJ50153), Ningbo Natural Science Foundation (No. 202003N4006), and the Joint Research Funds of the Department of Science & Technology of Shaanxi Province,

Northwestern Polytechnical University (No. 2020GXLH-Z-017).

REFERENCES

- (1) Saleh, T. A.; Sari, A.; Tuzen, M. Effective adsorption of antimony(III) from aqueous solutions by polyamide-graphene composite as a novel adsorbent. *Chem. Eng. J.* **2017**, *307*, 230–238.
- (2) Bocca, B.; Pino, A.; Alimonti, A.; Forte, G. Toxic metals contained in cosmetics: A status report. *Regul. Toxicol. Pharmacol.* **2014**, *68*, 447–467.
- (3) Nishad, P. A.; Bhaskarapillai, A. Antimony, a pollutant of emerging concern: A review on industrial sources and remediation technologies. *Chemosphere* **2021**, *277*, No. 130252.
- (4) Wu, Z.; He, M.; Guo, X.; Zhou, R. Removal of antimony (III) and antimony (V) from drinking water by ferric chloride coagulation: Competing ion effect and the mechanism analysis. *Sep. Purif. Technol.* **2010**, *76*, 184–190.
- (5) Sun, W.; Xiao, E.; Kalin, M.; Krumins, V.; Dong, Y.; Ning, Z.; Liu, T.; Sun, M.; Zhao, Y.; Wu, S.; Mao, J.; Xiao, T. Remediation of antimony-rich mine waters: Assessment of antimony removal and shifts in the microbial community of an onsite field-scale bioreactor. *Environ. Pollut.* **2016**, *215*, 213–222.
- (6) Nishiyama, S.-y.; Saito, K.; Sugita, K.; Sato, K.; Akiba, M.; Saito, T.; Tsuneda, S.; Hirata, A.; Tamada, M.; Sugo, T. High-speed recovery of antimony using chelating porous hollow-fiber membrane. *J. Membr. Sci.* **2003**, *214*, 275–281.
- (7) Bergmann, M. E. H.; Koparal, A. S. Electrochemical antimony removal from accumulator acid: Results from removal trials in laboratory cells. *J. Hazard. Mater.* **2011**, *196*, 59–65.
- (8) Fan, H.-T.; Sun, W.; Jiang, B.; Wang, Q.-J.; Li, D.-W.; Huang, C.-C.; Wang, K.-J.; Zhang, Z.-G.; Li, W.-X. Adsorption of antimony(III) from aqueous solution by mercapto-functionalized silica-supported organic–inorganic hybrid sorbent: Mechanism insights. *Chem. Eng. J.* **2016**, *286*, 128–138.
- (9) Wang, H.; Gao, B.; Wang, S.; Fang, J.; Xue, Y.; Yang, K. Removal of Pb(II), Cu(II), and Cd(II) from aqueous solutions by biochar derived from KMnO₄ treated hickory wood. *Bioresour. Technol.* **2015**, *197*, 356–362.
- (10) Peng, W.; Li, H.; Liu, Y.; Song, S. A review on heavy metal ions adsorption from water by graphene oxide and its composites. *J. Mol. Liq.* **2017**, *230*, 496–504.
- (11) d'Halluin, M.; Rull-Barrull, J.; Bretel, G.; Labrugère, C.; Le Grogne, E.; Felpin, F.-X. Chemically Modified Cellulose Filter Paper for Heavy Metal Remediation in Water. *ACS Sustainable Chem. Eng.* **2017**, *5*, 1965–1973.
- (12) Li, J.; Xing, X.; Li, J.; Shi, M.; Lin, A.; Xu, C.; Zheng, J.; Li, R. Preparation of thiol-functionalized activated carbon from sewage sludge with coal blending for heavy metal removal from contaminated water. *Environ. Pollut.* **2018**, *234*, 677–683.
- (13) Saleem, A.; Chen, J.; Liu, M.; Liu, N.; Usman, M.; Wang, K.; Haris, M.; Zhang, Y.; Li, P. Versatile Magnetic Mesoporous Carbon Derived Nano-Adsorbent for Synchronized Toxic Metal Removal and Bacterial Disinfection from Water Matrices. *Small* **2023**, *19*, No. 2207348.
- (14) Zhuang, W.; Gao, X. Assessment of heavy metal impact on sediment quality of the Xiaoqinghe estuary in the coastal Laizhou Bay, Bohai Sea: Inconsistency between two commonly used criteria. *Marin. Pollut. Bull.* **2014**, *83*, 352–357.
- (15) Liu, E.; Shen, J. A comparative study of metal pollution and potential eco-risk in the sediment of Chaohu Lake (China) based on total concentration and chemical speciation. *Environ. Sci. Pollut. Res.* **2014**, *21*, 7285–7295.
- (16) Li, J. Risk Assessment of Heavy Metals in Surface Sediments from the Yanghe River, China. *Int. J. Environ. Res. Public Health* **2014**, *11*, 12441–12453.
- (17) Shreadah, M. A.; Shobier, A. H.; Ghani, S. A. A.; El Zokm, G. M.; Said, T. O. Major ions anomalies and contamination status by trace metals in sediments from two hot spots along the Mediterranean Coast of Egypt. *Environ. Monit. Assess.* **2015**, *187*, 280.
- (18) Saleh, T. A.; Tuzen, M.; Sari, A. Effective antimony removal from wastewaters using polymer modified sepiolite: Isotherm kinetic and thermodynamic analysis. *Chem. Eng. Res. Des.* **2022**, *184*, 215–223.
- (19) Abdel -Aty, A. M.; Ammar, N. S.; Abdel Ghafar, H. H.; Ali, R. K. Biosorption of cadmium and lead from aqueous solution by fresh water alga *Anabaena sphaerica* biomass. *J. Adv. Res.* **2013**, *4*, 367–374.
- (20) Saranya, K.; Sundaramanickam, A.; Shekhar, S.; Meena, M.; Sathishkumar, R. S.; Balasubramanian, T. Biosorption of multi-heavy metals by coral associated phosphate solubilising bacteria *Cronobacter muytjensii* KSCAS2. *J. Environ. Manage.* **2018**, *222*, 396–401.
- (21) Karimpour, M.; Ashrafi, S. D.; Taghavi, K.; Mojtahedi, A.; Roohbakhsh, E.; Naghipour, D. Adsorption of cadmium and lead onto live and dead cell mass of *Pseudomonas aeruginosa*: A dataset. *Data Brief* **2018**, *18*, 1185–1192.
- (22) Bachate, S. P.; Nandre, V. S.; Ghatpande, N. S.; Kodam, K. M. Simultaneous reduction of Cr(VI) and oxidation of As(III) by *Bacillus firmus* TE7 isolated from tannery effluent. *Chemosphere* **2013**, *90*, 2273–2278.
- (23) Arivalagan, P.; Singaraj, D.; Haridass, V.; Kaliannan, T. Removal of cadmium from aqueous solution by batch studies using *Bacillus cereus*. *Ecol. Eng.* **2014**, *71*, 728–735.
- (24) Saleem, A.; Wang, J.; Sun, T.; Sharaf, F.; Haris, M.; Lei, S. Enhanced and selective adsorption of Copper ions from acidic conditions by diethylenetriaminepentaacetic acid-chitosan sewage sludge composite. *J. Environ. Chem. Eng.* **2020**, *8*, No. 104430.
- (25) Cheng, M.; Fang, Y.; Li, H.; Yang, Z. Review of recently used adsorbents for antimony removal from contaminated water. *Environ. Sci. Pollut. Res.* **2022**, *29*, 26021–26044.
- (26) Bai, Y.; Tang, X.; Sun, L.; Yin, W.; Hu, G.; Liu, M.; Gong, Y. Application of iron-based materials for removal of antimony and arsenic from water: Sorption properties and mechanism insights. *Chem. Eng. J.* **2022**, *431*, No. 134143.
- (27) Li, S. Q.; Zhou, P. J.; Chen, S. A Series of Nanocomposites of Chitosan/Rectorite: Preparation, Characterization and Application for Adsorption of Cu(II), Pb(II) and Cd(II). *Asian J. Chem.* **2013**, *25*, 9822–9828.
- (28) Saleem, A.; Zhang, Y.; Usman, M.; Haris, M.; Li, P. Tailored architectures of mesoporous carbon nanostructures: From synthesis to applications. *Nano Today* **2022**, *46*, No. 101607.
- (29) Liu, P.; Jiang, L.; Zhu, L.; Wang, A. Novel Covalently Cross-Linked Attapulgite/Poly(acrylic acid-co-acrylamide) Hybrid Hydrogels by Inverse Suspension Polymerization: Synthesis Optimization and Evaluation as Adsorbents for Toxic Heavy Metals. *Indus. Eng. Chem. Res.* **2014**, *53*, 4277–4285.
- (30) Jadhav, S. A.; Patil, V. S.; Shinde, P. S.; Thoravat, S. S.; Patil, P. S. A short review on recent progress in mesoporous silicas for the removal of metal ions from water. *Chem. Pap.* **2020**, *74*, 4143–4157.
- (31) Feng, J.; She, X.; He, X.; Zhu, J.; Li, Y.; Deng, C. Synthesis of magnetic graphene/mesoporous silica composites with boronic acid-functionalized pore-walls for selective and efficient residue analysis of aminoglycosides in milk. *Food Chem.* **2018**, *239*, 612–621.
- (32) Wang, H.; Liu, Y.; Yao, S.; Zhu, P. Selective recognition of dicyandiamide in bovine milk by mesoporous silica SBA-15 supported dicyandiamide imprinted polymer based on surface molecularly imprinting technique. *Food Chem.* **2018**, *240*, 1262–1267.
- (33) Huang, L.; Wu, J.; Liu, M.; Mao, L.; Huang, H.; Wan, Q.; Dai, Y.; Wen, Y.; Zhang, X.; Wei, Y. Direct surface grafting of mesoporous silica nanoparticles with phospholipid choline-containing copolymers through chain transfer free radical polymerization and their controlled drug delivery. *J. Colloid Interface Sci.* **2017**, *508*, 396–404.
- (34) Gao, B.; Jiang, G.; An, F. Preparation of iminodiacetic acid-type composite chelating material IDAA-PGMA/SiO₂ and preliminary studies on adsorption behavior of heavy metal ions and rare earth ions. *J. Appl. Polym. Sci.* **2012**, *125*, 2529–2538.
- (35) Shen, D.; Yang, J.; Li, X.; Zhou, L.; Zhang, R.; Li, W.; Chen, L.; Wang, R.; Zhang, F.; Zhao, D. Biphasic Stratification Approach to Three-Dimensional Dendritic Biodegradable Mesoporous Silica Nanospheres. *Nano Lett.* **2014**, *14*, 923–932.

- (36) Qi, J. J.; Xu, D. Y.; Cai, Q.; Wei, Z. Preparation and Characterization of Radially Porous Silica and the Core-shell Structure. *Chem. J. Chin. Univer.* **2012**, *33*, 652–656.
- (37) Croissant, J. G.; Butler, K. S.; Zink, J. I.; Brinker, C. J. Synthetic amorphous silica nanoparticles: toxicity, biomedical and environmental implications. *Nat. Rev. Mater.* **2020**, *5*, 886–909.
- (38) Hernández-Morales, V.; Nava, R.; Acosta-Silva, Y. J.; Macías-Sánchez, S. A.; Pérez-Bueno, J. J.; Pawelec, B. Adsorption of lead (II) on SBA-15 mesoporous molecular sieve functionalized with $-NH_2$ groups. *Microporous Mesoporous Mater.* **2012**, *160*, 133–142.
- (39) Chang, J.-S.; Kong, Z. L.; Hwang, D. F.; Chang, K. L. B. Chitosan-Catalyzed Aggregation during the Biomimetic Synthesis of Silica Nanoparticles. *Chem. Mater.* **2006**, *18*, 702–707.
- (40) Gao, Q.; Xu, W.; Xu, Y.; Wu, D.; Sun, Y.; Deng, F.; Shen, W. Amino Acid Adsorption on Mesoporous Materials: Influence of Types of Amino Acids, Modification of Mesoporous Materials, and Solution Conditions. *J. Phys. Chem. B.* **2008**, *112*, 2261–2267.
- (41) Tarley, C. R. T.; Andrade, F. N.; Santana, H.; Zaia, D. A. M.; Beijo, L. A.; Segatelli, M. G. Ion-imprinted polyvinylimidazole-silica hybrid copolymer for selective extraction of Pb(II): Characterization and metal adsorption kinetic and thermodynamic studies. *React. Funct. Polym.* **2012**, *72*, 83–91.
- (42) Guo, X.; Deng, Y.; Tu, B.; Zhao, D. Facile Synthesis of Hierarchically Mesoporous Silica Particles with Controllable Cavity in Their Surfaces. *Langmuir* **2010**, *26*, 702–708.
- (43) Cui, H. Z.; Li, Y. L.; Liu, S.; Zhang, J. F.; Zhou, Q.; Zhong, R.; Yang, M. L.; Hou, X. F. Novel Pb(II) ion-imprinted materials based on bis-pyrazolyl functionalized mesoporous silica for the selective removal of Pb(II) in water samples. *Microporous Mesoporous Mater.* **2017**, *241*, 165–177.
- (44) Zhou, L.; Wang, R.; Feng, W.; Li, Y.; Zhou, Y.; Luo, X.; Wang, L.; Yu, Q.; Chen, Z. Preparation of Thiohydroxy Modified Magnetic Mesoporous Silica from Rice Husk and its Removal Properties for Cd(II). *J. Food Sci. Biotechnol.* **2018**, *37*, 33–39.
- (45) Fu, M.; Zhong, X.; Lian-ming, X.; De-zhi, C. Preparation and its adsorption performance of heavy metal ions on mesoporous silica crosslinked chitosan composite. *Chem. Res. Appl.* **2016**, *28*, 1366–1370.
- (46) He, J. L.; Chen, X. H.; Zhu, W. J.; Ma, W. H.; Xiao, Y. Y.; Li, J.; Zhang, H. Synthesis of Mesoporous Silica Microspheres by PICA and Pseudomorphic Transformation Using Silica Fume as Silica Source. *Mater. Sci. Forum* **2014**, *809–810*, 207–212.
- (47) Li, J.; Chen, L.; Li, X.; Zhang, C.; Jiang, Y. One-step synthesis of structure controlled vinyl functionalized hollow mesoporous silica nanospheres. *New J. Chem.* **2015**, *39*, 287–294.
- (48) Zhou, L. *Modification of Magnetic Mesoporous Silica Using Rice Husk and Study on Adsorption Effect of Cadmium*. Master; Jiangnan University: Wuxi, 2017.